Applied Physics A (2020) 126:795
https://doi.org/10.1007/s00339-020-03976-7

Applied Physics A
Materials Science & Processing

S.I. : CURRENT STATE-OF-THE-ART IN LASER ABLATION

Ultrafast pump-probe microscopic imaging of femtosecond laser-induced melting and ablation in single-crystalline silicon carbide

D. Satoh[1,2] · T. Shibuya[1] · E. Terasawa[2,3] · Y. Moriai[2] · H. Ogawa[1,2] · M. Tanaka[1,2] · Y. Kobayashi[2,4] · R. Kuroda[1,2]

Received: 15 October 2019 / Accepted: 4 September 2020 / Published online: 18 September 2020

Abstract

The temporal and spatial evolution of femtosecond laser-induced phase transitions and ablation on single-crystalline silicon carbide (SiC) were investigated via pump-probe microscopy in air on a time scale from approximately 100 fs to 1 ns. The largest reflectivity change was observed between 300 fs and 1 ps after excitation, which is due to free carrier generation, and the Drude model calculations indicated that the maximum free electron density was greater than 3.3×10^{21} cm^{-3}. After a few picoseconds, there was direct evidence of the production of a rarefaction wave propagating towards the bulk, whose propagation velocity was estimated to be 3286 m/s. At delay times between a few hundreds of picoseconds and 1 ns, characteristic transient ring patterns were clearly observed and were related to the optical interference of the probe laser pulse reflected at the front surface of the ablating layer and at the interface of the non-ablating substrate. The estimated expansion velocity of the ablation front in 6H–SiC was found to be comparable to or slower than those reported for other semiconductors and dielectrics.

Keywords Ultrafast pump-probe microscopy · Silicon carbide · Laser-induced phase transition · Laser ablation

1 Introduction

Silicon carbide (SiC) has attracted considerable attention owing to its excellent properties, such as wide bandgap (~3 eV), high electric field breakdown strength (< 1 MV/cm), and high thermal conductivity (~4.9 W/cm·K). In particular, SiC is expected to be applicable to high power electronic devices in many industrial fields (e.g., radar communication, microelectronics, microwave, and aerospace fields [1–4]). In addition to the above characteristics, SiC has chemical stability, high heat resistance, and high wear resistance. However, owing to the hardness of SiC, there are issues in wafer dicing [5]. Femtosecond laser processing is expected to enable hyperfine dicing of SiC [5, 6], because it is a non-contact cutting technique that can be performed both locally and at a low controllable energy transfer level [7–9]. In terms of other applications, it is known that femtosecond laser irradiation of SiC can dramatically increase the local conductivity of SiC substrates [10–12]. This femtosecond laser modification technique for SiC enables the fabrication of three-dimensional electric circuits in SiC [10–12]. Recently, it has been found that the silicon-vacancy defect V_{Si} in a SiC substrate works as a single-photon source [13]. Furthermore, it has been reported that the electron spin of V_{Si} can be controlled at room temperature [14]. Research on the production of V_{Si} in SiC by femtosecond laser irradiation has also begun [12] and can contribute to the promotion of spintronics and quantum sensing technologies.

As mentioned above, many applications of femtosecond laser processing to SiC have been proposed and studied. To promote these technologies, the melting and laser ablation

✉ D. Satoh
dai-satou@aist.go.jp

1 Research Institute for Measurement and Analytical Instrumentation (RIMA), National Metrology Institute of Japan (NMIJ), National Institute of Advanced Industrial Science and Technology (AIST), 1-1-1 Umezono, Tsukuba 305-8568, Japan

2 AIST-UTokyo Advanced Operando-Measurement Technology Open Innovation Laboratory (OPERANDO-OIL), National Institute of Advanced Industrial Science and Technology (AIST), 5-1-5 Kashiwanoha, Kashiwa, Chiba 277-8589, Japan

3 Research Institute for Science and Engineering, Waseda University, 3-4-1 Okubo, Shinjuku, Tokyo 169-8555, Japan

4 The Institute for Solid State Physics, The University of Tokyo, 5-1-5 Kashiwanoha, Kashiwa, Chiba 277-8581, Japan

of SiC caused by femtosecond laser irradiation must be characterised consistently with sufficient spatial and temporal resolutions.

Pump-probe microscopy has been used to investigate the laser-induced phase transitions and ablation of some metals [15–19], semiconductors [15–17, 20–25], and dielectrics [15, 26–30] and is recognised as an effective measurement tool capable of observing ultrafast dynamics. The observation of transient phenomena after the photoexcitation of various materials using a pump-probe microscope and a hydrodynamic model of material ablation have provided an understanding of the physical process from excitation to surface ablation as follows. First, immediately after photoexcitation, the excited top-surface layer is isothermally heated to a temperature and pressure well above the critical point. This layer then undergoes adiabatic expansion, resulting in the propagation of a rarefaction wave from the surface into the bulk. When the rarefaction wave reaches the boundary with the unexcited part, it is reflected, and its propagation direction is reversed. Subsequently, during the expansion of this layer, liquid and gas coexist, resulting in a rapid decrease in the propagation velocity of the rarefaction wave. Eventually, the expanding material is believed to have a shell-like structure and an internal state formed by a mixture of liquids and gases. These depictions are consistent with the observations of several metals, semiconductors, and dielectrics. Recently, indicating the formation of a second ablation front, which has a very slow propagation velocity in $LiNbO_3$ [30], has been reported; yet, some points remain unclear. Observation of transient phenomena after photoexcitation in various materials is essential to understand the surface ablation mechanism in more detail. In this paper, we report a detailed study of the femtosecond laser-induced phase transitions and ablation dynamics of a single-crystalline SiC, which is a wide bandgap semiconductor, using pump-probe microscopy.

2 Experimental configuration

Figure 1 shows a schematic diagram of the ultrafast time-resolved imaging apparatus. This apparatus is developed based on a combination of pump-probe and wide-field microscopy to observe the temporal evolution of the reflectivity on the laser-excited surface with high spatial resolution. The chirped pulse regenerative laser amplifier system used for the pump-probe microscopy experiments provides linearly polarised pulses of 70 fs duration at a central wavelength of 800 nm. The laser pulses are divided into pump and probe pulses using the combination of a half-wave plate (HWP1) and a thin film polariser (TFP1) to adjust the pulse energy ratio between the pulses.

The combination of a second half-wave plate (HWP2) and thin film polariser (TFP2) is used to adjust the pump pulse energy to initiate the laser modification. The *p*-polarized pump laser pulse is focussed by a lens (CL1) at an angle of incidence of 45° onto the sample surface with respect to the microscope objective to avoid clipping. The elliptical beam waist of the pump laser pulse at the sample surface was measured using the method described by Liu [31–33]. The

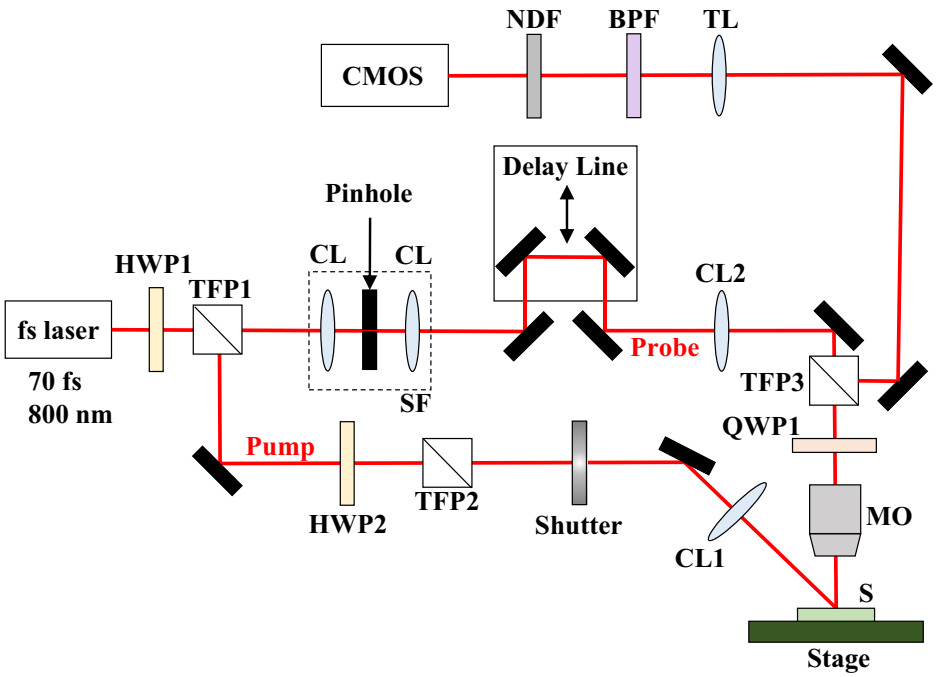

Fig. 1 Schematic of the ultrafast time-resolved imaging apparatus. Abbreviations: *S* sample, *HWP* half-wave plate, *QWP* quarter-wave plate, *TFP* thin film polarizer, *CL* convex lens, *MO* microscope objective, *SF* spatial filter, *TL* tube lens, *BPF* bandpass filter, *NDF* absorptive neutral density filter

obtained beam waist radii were $w_x = 53$ µm and $w_y = 19$ µm with an ellipticity of $w_y/w_x = 0.36$ on the sample surface. The threshold fluence for laser modification estimated from this Liu plot is 0.69 J/cm^2, which roughly matches the threshold fluence for the formation of amorphous SiC [12].

A spatial filter containing a tungsten pinhole (50 µm diameter) and two convex lenses was employed after the TFP1 to make the spatial beam profile of the probe pulse Gaussian. The time delay between the pump and probe pulses can be varied up to 1.5 ns by an optical delay line on a 200 mm translation stage. A convex lens (CL2) in front of a thin film polariser (TFP3) focuses the probe laser pulse to the parfocal plane of a microscope objective (10x, NA = 0.28, and 34.0 mm working distance), resulting in collimated illumination of the sample surface at normal incidence. The polarisation of the probe laser pulse reflected from the sample surface is turned by 90° in total by passing a second time through QWP1 and then is reflected at TFP3 towards the complementary metal–oxide–semiconductor (CMOS) camera. A bandpass filter (BPF) centred at 800 nm is placed in the imaging path to eliminate most of the plasma light emission. To reduce the detection ratio of the scattered pump light from the sample surface, an absorptive neutral density filter (NDF) is also used. A tube lens (TL, $f = 200$ mm) focuses the probe laser pulse onto the 12-bit CMOS camera for imaging. This 12-bit CMOS camera with 4096 × 2160 pixels provides a pixel resolution of 0.35 µm in this configuration.

As found in previous research [30], pump-probe microscopic imaging using a single wavelength is difficult, because the pump and probe pulses cannot be distinguished spectrally. Most of the scattered light derived from the pump pulse is separated by the polariser. However, some of it cannot be completely removed. Consequently, the intensity of the probe pulse was increased within a range that did not affect the sample surface to improve the signal-to-noise ratio. It has been tested that the probe pulse does not affect the laser modification produced on the sample surface either by itself or in combination with the pump pulse.

Time zero is defined as the delay time setting, where perfect temporal overlap between the pump and probe laser pulses on the sample surface is established. In this system, time zero was determined from the relationship between the pump-probe time delay and the surface modification of the sample irradiated by both the pump and probe laser pulses. If the pump and probe laser pulses overlap on the sample surface, a clear interference pattern is generated in the area affected by laser irradiation owing to the interference effect of these two laser pulses. In this system, the delay time at which the clearest interference pattern was observed on the sample surface was defined as time zero.

A pump-probe microscopy experiment was performed with single-pulsed laser irradiation on a 6H–SiC (0001) wafer with a thickness of 330 µm, which was cut in a 10.5 × 10.5 mm square. This pump-probe transient reflectivity measurement was performed with a probe laser fluence well below the laser-induced damage threshold, whereas the laser fluence of the pump pulse was sufficient to induce phase transitions such as melting or ablation. The pump pulse energies were measured using a pyroelectric energy sensor at the sample site. The laser-induced reflectivity change $\Delta R(\tau, x_0, y_0)$ corresponding to different pump and probe pulse delays τ was calculated from three measurement images. The first measurements were obtained from a reflectivity image $R_0(\tau, x, y)$ of the non-excited sample surface at the measurement position. The second measurements, which were of the surface reflectivity $R(\tau, x, y)$ upon pump pulse excitation, were recorded at the same measurement position. To estimate the background noise due to the scattered pump pulse, images of the scattered pump light $R_{\mathrm{scatt}}(x, y)$ were obtained only by pump pulse irradiation. The amount of background noise due to scattered pump pulses $\overline{R_{\mathrm{scatt}}}(x_0, y_0)$ was estimated by calculating the average reflectivity change from the pixel data near the evaluation point (x_0, y_0) in the $R_{\mathrm{scatt}}(x, y)$ images. Therefore, the laser-induced reflectivity change $\Delta R(\tau)/R_0(\tau)$ was calculated using the following equation:

$$\frac{\Delta R(\tau)}{R_0(\tau)} \equiv \frac{R(\tau, x_0, y_0) - R_0(\tau, x_0, y_0) - \overline{R_{\mathrm{scatt}}}(x_0, y_0)}{R_0(\tau, x_0, y_0)}.$$

3 Results and discussion

Figure 2 presents a series of picture frames representing time-resolved surface reflection images obtained using 6H–SiC samples. These images reveal the change in the surface reflectivity after irradiation by a single pump pulse at a peak fluence of 2.15 J/cm^2. The time indicated in each frame is the delay time between the pump and probe laser pulses. The area excited by the pump laser irradiation has an elliptical shape because the incident angle of the pump laser pulse was 45° from the surface normal. The pump laser pulse was incident from the left side. Figure 3a shows an image of the final modification on the sample surface acquired by a laser confocal microscope. Figure 3b shows a vertical profile of the final modification along the red dashed line. From Fig. 3a and b, slight surface structures were found at the centre of the crater bottom. In addition to the formation of the crater, an increase in reflectivity is observable in the layer below the surface of the ablation region, suggesting that the optical properties of this layer were modified. To follow quantitatively the time evolution of the relative reflectivity of the 6H–SiC surface by pump laser irradiation, Fig. 4 depicts the normalised surface reflectivity change

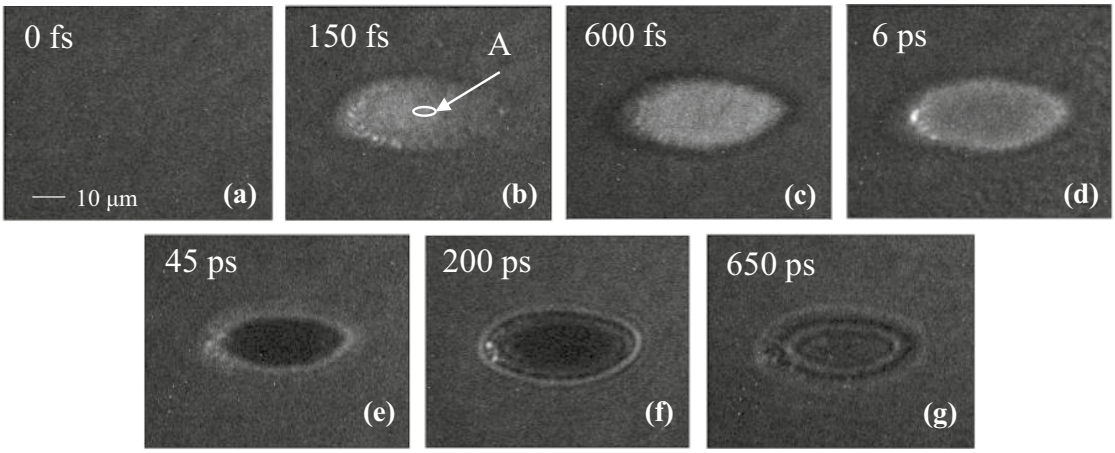

Fig. 2 **a**–**g** Time-resolved microscopy images of SiC surface at different time delays after excitation by a pump laser pulse (pump fluence 2.15 J/cm^2, ablation regime)

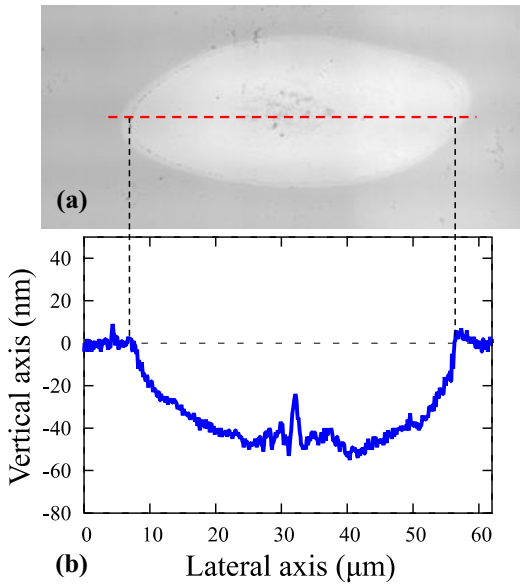

Fig. 3 **a** Image of SiC surface after laser irradiation acquired by a laser confocal microscope. **b** Vertical profile of the ablation crater along the red dashed line

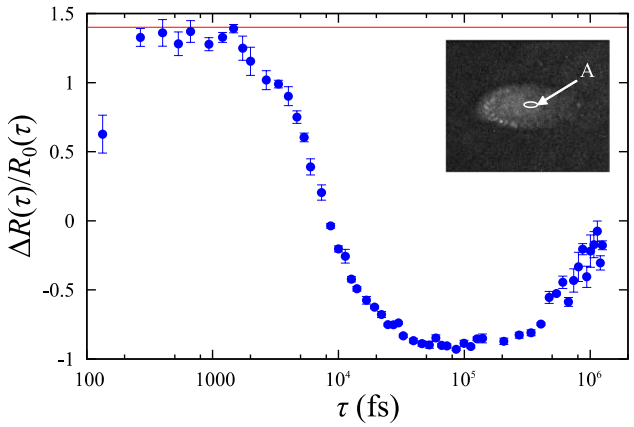

Fig. 4 Normalized surface reflectivity change $\Delta R(\tau)/R_0(\tau)$ at the centre point A (centre of the change region) as a function of the delay time τ. The red line shows the value of $\Delta R/R_0 = 1.4$ at which the reflectivity change became maximum

$\Delta R(\tau)/R_0(\tau)$ as a function of the delay time τ. The evaluation point (x_0, y_0) of $\Delta R(\tau)/R_0(\tau)$ plotted in Fig. 4 is the centre point A of the irradiation spots shown in Fig. 2b.

The following subsections detail the reflectivity changes and related physical processes in various time ranges.

3.1 Generation of free carriers (150 fs < τ < 1 ps)

First, a reflectivity increase surrounded by an annular decrease is observable at delays of 150 fs and 600 fs in Fig. 2b and c, respectively. In terms of the reflectivity change at the centre point A, the increase in reflectivity is saturated at $\Delta R(\tau)/R_0(\tau) \sim 1.4$–300 fs after excitation, and this value remains until approximately 1 ps. This phenomenon could have been caused by free carrier generation due to the high-intensity laser irradiation. To estimate the electron density induced in our experiments, the evolution of the surface reflectivity of 6H–SiC was calculated as a function of the electron density n_e using the Drude model for a free electron gas. The optical reflectivity of the air–material interface for a given density of free carriers at normal incidence is given by the Fresnel equation [26, 34]:

$R = \left|\frac{k_1 - k_2}{k_1 + k_2}\right|^2$, where the wave vectors k_1 and k_2 are given by ${k_1}^2 = \omega^2\mu\varepsilon = (n\omega/c)^2$ and ${k_2}^2 = (\omega/c)^2[n^2 - (\omega_p/\omega)^2(1 + i/\omega\tau_D)^{-1}]$ and ${\omega_p}^2 = n_e e^2/m_{\text{eff}}\varepsilon_0$, where ω is the frequency of the probe pulse ($\lambda = 800$ nm), $n = 2.60$ the refractive index of the

6H–SiC at the probe pulse wavelength [35], c is the speed of light in a vacuum, ε_0 is the vacuum dielectric permittivity, and e is the electron charge. For 6H–SiC, we used the effective electron mass $m_{\text{eff}} = 0.24\ m_e$ (m_e denotes the free electron mass) and Drude damping time $\tau_D = 3.9$ fs, following the argument in Refs. [36, 37].

Figure 5 shows the calculated surface reflectivity change of 6H–SiC as a function of the free electron density obtained using the Drude model. The transient electron density corresponding to the maximum value of the experimental reflectivity change $\Delta R/R_0$ (300 fs $< \tau <$ 1 ps) ~ 1.4 on the 6H–SiC surface is approximately 3.3×10^{21} cm^{-3}. It should be noted, however, that ablation may counteract the reflectivity increase produced by the free electron plasma, resulting in underestimation of the free electron density. It should also be considered that the Drude damping time τ_D is inversely proportional to the electron temperature [38]. In the photoexcited state with ablation, as in this experiment, the Drude damping time was estimated to be even shorter than the above representative value owing to the high electron temperature. In addition, the fact that the electron density is inversely proportional to the Drude damping time [26] indicates that the actual photo-generated carrier density could be higher than the calculated value (3.3×10^{21} cm^{-3}). It is theoretically suggested that instability of the lattice structure can occur within less than a few hundred femtoseconds, directly leading to very rapid melting of the crystal structure if the critical density in the conduction band exceeds 10^{21}–10^{22} cm^{-3} [39]. This laser-induced ultrafast phase transition is usually referred to as non-thermal melting and has already been reported in some semiconductors [22, 23]. Therefore, non-thermal melting may have occurred on the 6H–SiC surface in this time range.

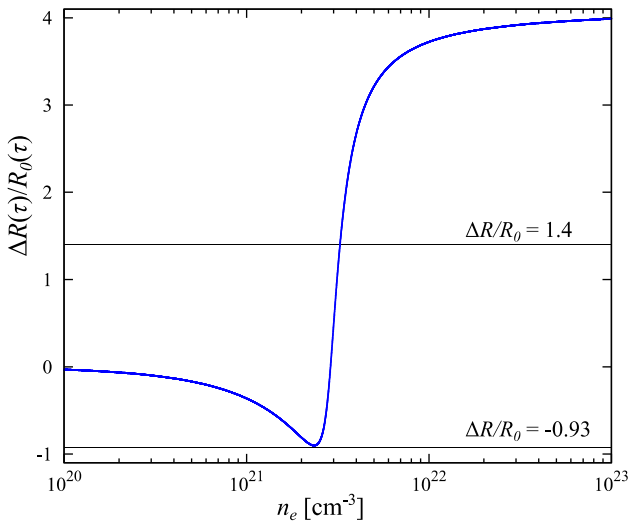

Fig. 5 Calculated surface reflectivity change of 6H–SiC as a function of the free electron density using the Drude model. The effective electron mass m_{eff} and Drude damping time τ_D are $m_{\text{eff}} = 0.24\ m_e$ and $\tau_D = 3.9$ fs, respectively [36, 37]. The black lines represent the measured maximum ($\Delta R/R_0 = 1.4$) and minimum ($\Delta R/R_0 = -0.93$) values of the reflectivity change at the centre point A of the excitation region

3.2 Relaxation of free carriers/propagation of a rarefaction wave (1 ps < τ < a few tens of picoseconds)

A few picoseconds after the pump pulse irradiation, a decrease in the surface reflectivity is observable across the pump area. Figure 4 shows that this decrease in reflectivity at the centre point A is below the initial value at 8.5 ps after pump pulse irradiation, and eventually the reflectivity change $\Delta R(\tau)/R_0(\tau)$ decreases to -0.93. Two physical mechanisms may be responsible for this reflectivity reduction.

The first mechanism is the free electron density reduction caused by inelastic scattering with the lattice. The Drude model calculations shown in Fig. 5 suggest that the reflectivity change becomes negative when the electron density is approximately 2.9×10^{21} cm^{-3}. Furthermore, when the electron density is about 2.4×10^{21} cm^{-3}, the reflectivity change decreases to a minimum of approximately -0.9. This phenomenon is also observable in the earlier time region (e.g., $\tau = 600$ fs) as a ring-shaped decrease in reflectivity around the periphery of the central increase in reflectivity, as also observed in Fig. 2c. However, since the decrease in reflectivity here is slightly larger than that in Fig. 5, the influence of other physical phenomena is also suggested.

Another related phenomenon that can be considered is surface ablation. As described in the hydrodynamic model of material ablation, a homogeneously excited and thermalised thin layer occurs in the early stages of ablation, followed by adiabatic expansion [21]. At the end of the isochoric heating process, this layer reaches very high temperatures of several thousand Kelvin at tens of gigapascals of pressure [29]. In the 10–30 ps range, the expanding layer does not have time to exchange heat with the surrounding medium and is thought to exhibit optical properties similar to those of a high-temperature black body [29, 30]. Several experimental results consistent with this physical interpretation have been reported, including measurements of transient reflections and transient transmissions in various dielectrics [40, 41]. This experimental result, in which the decrease in reflectivity starts in a few picoseconds, is also consistent with the fact that the thermalisation of the carrier and lattice takes only a few picoseconds [17]. This experimental result may also support this hypothesis, as the reflectivity is close to zero. To confirm the presence of temporary black bodies, detailed assessments of the spectral properties of such a transient state of the material and surface emission [30] are required.

Although our experiments alone do not entirely clarify the mechanism leading to strong reflectivity reduction, there are relevant results that can help elucidate this phenomenon. Figure 6 shows the trend of the reflectivity change from approximately 1–50 ps at three different local fluences. It is worth noting that the reflectivity decreases monotonically, independent of the local fluence, in the range of a few picoseconds to 12 ps. This reflectivity decrease is thought to be direct experimental evidence for the production of propagating rarefaction waves after isochoric heating [30]. According to the thermodynamic model of material ablation [21], the rarefaction wave propagates from the surface to the interior of the bulk at the speed of sound in the material c_0 with adiabatic expansion after isochoric heating. This expanding layer has the same density gradient at different lateral positions because the propagation speed of the rarefaction wave is independent of the local fluence. Consequently, the optical property (reflectivity) does not show positional dependence.

The propagating rarefaction wave eventually reaches the backward boundary of the ablation layer (the interface between the heated layer and substrate). At this boundary, the rarefaction wave loses the flow velocity, and a density discontinuity occurs. It should be noted that the arrival time of the rarefaction wave depends on the lateral position because the thickness of the heated region depends on the fluence. In other words, the heated layer becomes thinner in the lower fluence region, so that the rarefaction wave reaches the interface with the substrate more quickly. The arrival of the rarefaction wave at the interface appears in the trend of reflectivity changes [30]. In our experimental results,

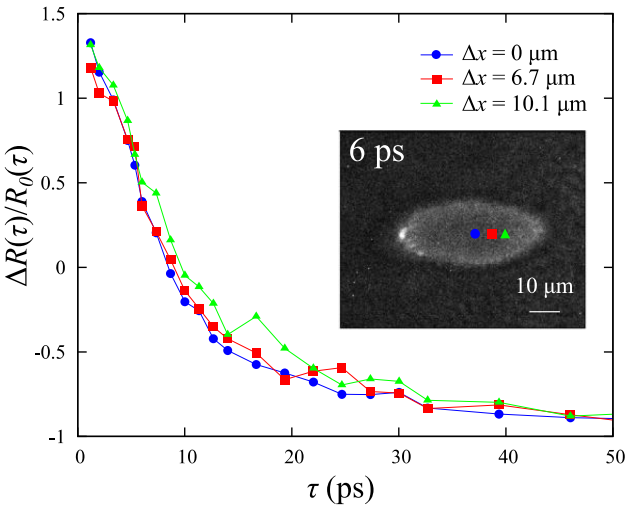

Fig. 6 Time evolution of reflectivity changes extracted from images at three different locations (each point on the photograph) on the excitation region. The long axis is x and the distance from the center of the irradiation (blue dot on the photograph) is defined as Δx. The red square and the green triangle indicate the positions of $\Delta x = 6.7$ μm and $\Delta x = 10.1$ μm, respectively

the reflectivity at $\Delta x = 6.7$ μm and $\Delta x = 10.1$ μm exhibits a slight increase in reflectivity at 14 ps and 19 ps, respectively, as shown in Fig. 6. The thickness of the heated layer was approximated to the final crater shape to estimate the propagation velocity of the rarefaction wave using the calculation method shown in Ref. [30]. The position of $\Delta x = 6.7$ μm corresponds to a slight uplift structure at the crater bottom as shown in Fig. 3b and was not used for this calculation. From the vertical profile of the ablation crater shown in Fig. 3b, the crater depth at $\Delta x = 10.1$ μm is 46 nm and the change in trend occurs at 14 ps, providing a propagation velocity of $c_0 = 46$ nm/14 ps = 3286 m/s. The obtained values are roughly around the speed of sound, which is consistent with the propagation velocity of the rarefaction wave in $LiNbO_3$ ($c_0 = 3200$–4100 m/s) observed in previous studies [30].

3.3 Expansion of the ablation layer (a few hundreds of picoseconds < τ < 1 ns)

At delay times between a few hundreds of picoseconds and 1 ns, characteristic transient ring patterns are clearly observable, as shown in Fig. 2f and g. The appearance of these ring patterns has been observed and studied in detail in other materials, such as Au, Ti, Si, Ge, GaAs, InP, SiO_2, and $LiNbO_3$ [15–30], which was caused by an optical interference effect. It is generally understood that the appearance and changes of such interference fringes result from the interference between the light reflected from the front of the dynamically moving ablation layer and the remaining surface underneath [16]. We attempted to estimate the actual velocity of the ablation front v from the temporal evolution of the order of the Newton rings [28]. First, the maximum "optical velocity" v_{opt} was calculated from the probe wavelength (800 nm) and the temporal evolution of the order of the Newton rings, yielding $v_{opt} \sim 900$ m/s. This value is approximately 30% lower than the optical velocity measured for bulk $LiNbO_3$ ($v_{opt} = 1170$–1400 m/s [28, 30]) after irradiation with a femtosecond laser pulse at comparable fluence. The actual velocity of the ablation front v is determined by the equation $v = v_{opt}/n_{eff}$, using the maximum optical velocity v_{opt} and unknown effective refractive index n_{eff} of the ablation layer. It has been experimentally proven that the ablation layer consists of an expanded two-phase liquid/gas region with a refractive index significantly reduced compared to that of the bulk material [28, 42]. Previous studies have indicated that v for some metals, semiconductors, and dielectrics is approximately 800 m/s [28, 42]. Even if the effective refractive index of the 6H–SiC ablation layer is also very small, it is likely that the value of v is similar to or less than it is for materials. The slow propagation of the ablation front can be related to the fact that the slow increase in reflectivity change continues even after 1 ns, as shown in Fig. 4. The reason that v is less than it is for other materials

may be that the pump depth position was slightly more internal than the top surface. When more deeply excited, the propagation velocity of the ablation front becomes slower because the inertia increases with the thickness of the material from the top surface [27]. This hypothesis will be clarified by obtaining transient reflection images by varying the irradiation depth and will be the subject of future work.

4 Conclusions

This study revealed, for the first time, the details of the spatial and temporal evolution of the dynamics of the excitation and ablation process of 6H–SiC upon irradiation with a single femtosecond laser pulse. In this experiment, the transient phenomena after optical pumping at a wavelength of 800 nm with a fluence higher than the ablation threshold were observed using a pump-probe microscope. At the sub-picosecond time scale, the maximum reflectivity change was observed, with values of $\Delta R(\tau)/R_0(\tau) \sim 1.4$. This phenomenon is due to the free carrier generation, and the Drude model calculations indicated that the maximum free electron density was greater than 3.3×10^{21} cm^{-3}. In the range of a few picoseconds to 12 ps, the observed monotonic reflectivity decrease, independent of the local fluence, is experimental evidence of the production of propagating rarefaction waves after isochoric heating. The propagation velocity of the rarefaction wave in the bulk was estimated to be $c_0 = 3286$ m/s, which is comparable to that of some metals and dielectrics. Characteristic ring patterns were observed in the time range of a few 100 ps–1 ns, indicating the onset of material expansion and ablation. The expansion velocity of the ablation front in 6H–SiC, estimated from the temporal evolution of the order of the Newton rings, was found to be comparable to or less than those reported for some metals, semiconductors, and dielectrics. These findings, obtained by observing the ablation dynamics of 6H–SiC, provide information regarding the optimisation of ultrafast laser structuring and will greatly contribute to the development of a wide variety of SiC applications.

Acknowledgements This work is partly based on results obtained from the New Energy and Industrial Technology Development Organization (NEDO) project "Development of advanced laser processing with intelligence based on high-brightness and high-efficiency laser technologies (TACMI project)."

References

1. S. Doğan, A. Teke, D. Huang, H. Morkoc, C.B. Roberts, J. Parish, B. Ganguly, M. Smith, R.E. Myers, S.E. Saddow, Appl. Phys. Lett. **82**, 3107 (2003)
2. Y. Shoji, K. Nakanishi, Y. Sakakibara, K. Kintaka, H. Kawashima, M. Mori, T. Kamei, Appl. Phys. Express **3**, 122201 (2010)
3. K. Ito, S. Tsukimoto, M. Murakami, Sci. Technol. Adv. Mater. **7**, 496 (2006)
4. M. Bhatnagar, B.J. Baliga, IEEE Trans. Electron. Dev. **40**, 645 (1993)
5. E. Kim, Y. Shimotsuma, M. Sakakura, K. Miura, Opt. Mater. Express **7**, 2450 (2017)
6. M. Farsari, G. Filippidis, S. Zoppel, G.A. Reider, C. Fotakis, J. Micromech. Microeng. **15**, 1786 (2005)
7. J. Bonse, S. Baudach, J. Kruger, W. Kautek, M. Lenzner, Appl. Phys. A **74**, 19 (2002)
8. H.O. Jeschke, M.E. Garcia, M. Lenzner, J. Bonse, J. Kruger, W. Kautek, Appl. Surf. Sci. **197**, 839 (2002)
9. T. Tomita, R. Kumai, H. Nomura, S. Matsuo, S. Hashimoto, K. Morita, T. Isu, Appl. Phys. A **105**, 89 (2011)
10. M. Deki, T. Ito, M. Yamamoto, T. Tomita, S. Matsuo, S. Hashimoto, T. Kitada, T. Isu, S. Onoda, T. Ohshima, Appl. Phys. Lett. **98**, 133104 (2011)
11. T. Ito, M. Deki, T. Tomita, S. Matsuo, S. Hashimoto, T. Kitada, T. Isu, S. Onoda, T. Ohshima, J. Laser Micro. Nanoeng. **7**, 16 (2012)
12. T. Tomita, M. Deki, E. Yanagita, Y. Bando, Y. Naoi, T. Makino, T. Ohshima, J. Laser Micro. Nanoeng. **12**, 72 (2017)
13. S. Castelletto, B.C. Johnson, V. Ivady, N. Stavrias, T. Umeda, A. Gali, T. Ohshima, Nat. Mater. **13**, 151 (2014)
14. D.J. Christle, A.L. Falk, P. Andrich, P.V. Klimov, J.U. Hassan, N.T. Son, E. Janźen, T. Ohshima, D.D. Awschalom, Nat. Materials **14**, 160 (2015)
15. D. von der Linde, K. Sokolowski-Tinten, J. Bialkowski, Appl. Surf. Sci. **109–110**, 1 (1997)
16. K. Sokolowski-Tinten, J. Bialkowski, A. Cavalleri, D. von der Linde, A. Oparin, J. Meyer-ter-Vehn, S.I. Anisimov, Phys. Rev. Lett. **81**, 224 (1998)
17. B. Rethfeld, V.V. Temnov, K. Sokolowski-Tinten, S.I. Anisimov, D. von der Linde, Proc. SPIE **4760**, 72 (2002)
18. M. Domke, S. Rapp, M. Schmidt, H.P. Huber, Opt. Express **20**, 10330 (2012)
19. T. Pflug, J. Wang, M. Olbrich, M. Frank, A. Horn, Appl. Phys. A **124**, 116 (2018)
20. M.C. Downer, R.L. Fork, C.V. Shank, J. Opt. Soc. Am. B **2**, 595 (1985)
21. D. von der Linde, K. Sokolowski-Tinten, Appl. Surf. Sci. **154–155**, 1 (2000)
22. J. Bonse, G. Bachelier, J. Siegel, J. Solis, Phys. Rev. B **74**, 134106 (2006)
23. K. Sokolowski-Tinten, J. Bialkowski, M. Boing, A. Cavalleri, D. von der Linde, Phys. Rev. B **58**, R11805 (1998)
24. J. Bonse, G. Bachlier, S.M. Wiggins, J. Siegel, J. Solis, J. Kruger, H. Sturm, J. Optoelectron. Adv. M. **12**, 421 (2010)
25. J. Bonse, G. Bachelier, J. Siegel, J. Solis, H. Sturm, J. Appl. Phys. **103**, 054910 (2008)
26. D. Puerto, J. Siegel, W. Gawelda, M. Galvan-Sosa, L. Ehrentraut, J. Bonse, J. Solis, J. Opt. Soc. Am. B **27**, 1065 (2010)
27. S. Rapp, M. Domke, M. Schmidt, H.P. Huber, Physics Procedia **41**, 734 (2013)
28. M. Garcia-Lechuga, J. Siegel, J. Hernandez-Rueda, J. Solis, Appl. Phys. Lett. **105**, 112902 (2014)
29. M. Garcia-Lechuga, L. Haahr-Lillevang, J. Siegel, P. Balling, S. Guizard, J. Solis, Phys. Rev. B **95**, 214114 (2017)
30. M. Garcia-Lechuga, J. Solis, J. Siegel, Appl. Phys. A **124**, 221 (2018)
31. J.M. Liu, Opt. Lett. **7**, 196 (1982)
32. N. Sanner, O. Utéza, B. Bussiere, G. Coustillier, A. Leray, T. Itina, M. Sentis, Appl. Phys. A **94**, 889 (2009)
33. A. Ben-Yakar, R.L. Byer, J. Appl. Phys. **96**, 5316 (2004)
34. M. Born, E. Wolf, *Principles of optics* (Pergamon, New York, 1980)
35. W.J. Choyke, L. Patrick, JOSA **58**, 377 (1968)

36. T.E. Tiwald, J.A. Woollam, S. Zollner, J. Christiansen, R.B. Gregory, T. Wetteroth, A.R. Powell, Phys. Rev. B **60**, 11464 (1999)
37. J. Song, W. Tao, H. Song, M. Gong, G. Ma, Y. Dai, Q. Zhao, J. Qiu, Appl. Phys. A **122**, 341 (2016)
38. S.A. Sato, Y. Shinohara, T. Otobe, K. Yabana, Phys. Rev. B **90**, 174303 (2014)
39. P. Stampfli, K.H. Bennemann, Phys. Rev. B **42**, 7163 (1990)
40. I.H. Chowdhury, A.Q. Wu, X. Xu, A.M. Weiner, Appl. Phys. A Mater. Sci. Process **81**, 1627 (2005)
41. D. Puerto, W. Gawelda, J. Siegel, J. Bonse, G. Bachelier, J. Solis, Appl. Phys. A Mater. Sci. Process **92**, 803 (2008)
42. K. Sokolowski-Tinten, J. Bialkowski, A. Cavalleri, M. Boing, H. Schuler, D. von der Linde, Proc. SPIE **3343**, 46 (1998)